JMEPEG (2018) 27:4655–4664
https://doi.org/10.1007/s11665-018-3569-2

1059-9495/$19.00

Influence of Laser Nitriding on the Surface and Corrosion Properties of Ti-20Nb-13Zr Alloy in Artificial Saliva for Dental Applications

Mohamed A. Hussein, Bekir Yilbas, A. Madhan Kumar, Robin Drew, and Nasser Al-Aqeeli

(Submitted January 22, 2018; in revised form July 31, 2018; published online August 17, 2018)

Ti alloys have been used for dentistry due to their lower density and improved compatibility. However, the resistance to corrosion and surface hardness of Ti alloys need to be improved to avoid the formation of debris, which affects the long-term biocompatibility. In the present work, the surface characteristics and corrosion protection in artificial saliva produced by laser nitriding of a new biomedical Ti-20Nb-13Zr at.% alloy have been investigated for dental applications. The laser nitrided and untreated alloy surfaces were examined using XRD, FE-SEM, x-ray photon spectroscopy, Vickers microhardness measurements, atomic force microscopy, scratch measurements, Raman spectroscopy, and surface energy measurements. The susceptibility of the laser nitrided TNZ alloy to corrosion in an artificial saliva medium was investigated by electrochemical corrosion tests, which were performed by utilizing open circuit potential monitoring, electrochemical frequency modulation, and electrochemical impedance spectroscopic methods. The findings revealed that a TiN layer formed on the alloy surface after nitriding. The surface hardness of the treated alloy was 2.4 times that of the as-received samples. Moreover, the results showed improved friction coefficient and hydrophilic surface characteristics. The corrosion analysis revealed that the compact and dense TiN layer produced during laser nitriding improved the corrosion resistance of the Ti-20Nb-13Zr sample in artificial saliva medium.

Keywords biomaterial, corrosion, laser surface treatment, titanium alloy

1. Introduction

Titanium and titanium-based alloys exhibit better biocompatibility characteristics than alloy systems such as stainless steels and Co-Cr; thus, they are preferred in medical and dentistry applications (Ref 1-3). Due to the improved biocompatibility of Ti and the Ti-based alloy TiAl6V4 (Ti64), they are selected for dental applications (Ref 4), though it has been reported that V and Al may exhibit toxicity (Ref 5). The Ti-Nb-Zr alloy consists of nontoxic and biocompatible elements (Ref 1, 2, 6, 7); however, titanium and titanium-based alloys exhibit low tribological resistance and corrosion (Ref 8, 9), which result in the formation of wear debris that leads to implant loss due to osteolysis (Ref 10). Hence, surface treatment and coating of Ti alloys are required to enhance their wear (Ref 11) and corrosion resistance (Ref 12).

Mohamed A. Hussein and **A. Madhan Kumar**, Center of Research Excellence in Corrosion, Research Institute, King Fahd University of Petroleum and Minerals (KFUPM), Dhahran 31261, Saudi Arabia; **Bekir Yilbas** and **Nasser Al-Aqeeli**, Department of Mechanical Engineering, King Fahd University of Petroleum and Minerals (KFUPM), Dhahran 31261, Saudi Arabia; and **Robin Drew**, Department of Mechanical and Industrial Engineering, Concordia University, Montreal H3G 1M8, Canada. Contact e-mail: naqeeli@kfupm.edu.sa.

Several coating and surface treatment methods to improve the corrosion and wear characteristics of biomaterials were recently reviewed (Ref 13). Among various surface modification techniques, laser surface treatments have arisen as a likely method for enhancing surface characteristics, such as resistance to wear and corrosion. More precisely, nitriding has been carried out for Ti64 alloy to enhance its dry wear resistance (Ref 14, 15), corrosion protection and wear properties (Ref 16, 17). Despite the various studies available on Ti-6Al-4V, limited work has been reported on the laser nitriding of TNZ (Ti-Nb-Zr) alloys, which consist of nontoxic elements and show potential for biomedical applications as an implant material (Ref 7). One of the few studies that examined the effect of laser nitriding on the corrosion performance of TNZ alloys was performed by Sathish et al. (Ref 15). They evaluated the impact of laser nitriding with different scanning rates on the surface hardness and corrosion performance and reported that laser nitriding increases the wear and corrosion protection of commercial Ti and Ti-13Nb-13Zr alloys. Recently, laser gas diffusion nitriding was used to enhance the surface characteristics of the Ti alloy (Ref 18). Geetha et al. evaluated the surface protective performance of laser nitriding on Ti-13Nb-13Zr alloys in a physiological medium and observed that the laser nitrided surface displayed improved corrosion resistant performance compared to bare surfaces (Ref 19). Man et al. (Ref 20) fabricated a TiN layer on Ti through laser nitriding and prepared a vase-shaped hole structure for improving implant fixation for dental applications.

TiN coatings have been shown to improve wear resistance, hardness, and biocompatibility (Ref 21). Moreover, they have good physical and chemical stability (Ref 22). Different nitriding processes, such as laser nitriding, plasma nitriding,

Table 1 Scratch test parameters

Parameter	Indenter tip radius	Initial load	Final load	Loading rate	Scratch length	Scanning speed
Value	100 μm	0.03 N	2.5 N	0.01 N s^{-1}	3 mm	5 mm min^{-1}

and ion implantation, were applied to enhance the wear characteristics of Ti alloys. Of these processes, laser nitriding is preferred because it results in improved bonding and interfacial properties with the base alloy compared to physical vapor deposition, ion implantation, and chemical vapor deposition, (Ref 23, 24). Therefore, we applied laser nitriding in this work to improve the material surface characteristics. Though TiN coatings on Ti have been reported for biomedical applications in simulated body fluids (Ref 12, 25, 26), their application in oral environments is quite limited.

In the current paper, laser gas-assisted treatment is carried out on the recently fabricated Ti-20Nb-13Zr at.% biomedical alloy to improve its surface characteristics and corrosion protection in artificial saliva for dental applications. Structure, microstructure, hardness, and surface energy analyses have been performed and their results compared for both the treated and base samples. The effect of laser nitriding on the corrosion protection in artificial saliva has been assessed.

2. Experiments

2.1 Laser Surface Nitriding

The substrate nitrided in the present work was a Ti-20Nb-13Zr at.% cylindrically shaped sample of 20 mm with a thickness of 3 mm, synthesized using mechanical alloying and then consolidated using spark plasma sintering. It consisted of a β-Ti (bcc) matrix surrounded by a nanograined α-Ti (hcp) region. The details of the fabrication method have been previously reported (Ref 7). Laser surface treatments were carried out using a CO_2 laser (LC-ALPHAIII) with a nominal output power of 2 kW. Nitrogen gas was continually purged during the laser treatment process from a conical nozzle and was co-axially purged with the laser beam based on prior research (Ref 27, 28). The parameters of laser processing were carefully optimized after primary tests as reported elsewhere (Ref 12).

2.2 Characterization Methods

An XRD instrument (AXSD8) was used to investigate the phases of the nitrided and untreated samples. The XRD parameters were set to 40 kV and 30 mA. The microstructure was examined using FE-SEM (Tescan Lyra-3). EDX analysis was performed on different positions of the treated alloy surface, and a surface analysis of the alloy was performed by XPS (ESCALAB 250 XI) with a 6.12×10^{-10} mbar base pressure. A Raman spectrometer from Thermo Scientific, Germany, with a laser power of 6 mW, a laser wavelength of 455 nm, and an estimated spot size of 0.6 μm was used to study the treated sample. AFM was used to illustrate the surface topography of the nitrided sample. The microhardness (HV) of the laser nitrided and as-received alloys was measured using a hardness tester with a 500-g load and a 10-s dwell time. We report average values obtained from ten different locations. The friction coefficients of the samples were characterized via a micro-scratch tester (MTR3/50-NI) using a Rockwell diamond indenter. This test was conducted at room temperature with the parameters shown in Table 1.

2.3 Surface Energy Determination

The sessile drop technique was adapted to analyze the contact angle at room temperature, with a droplet volume of 3 μL. The contact angle for 10 drops was measured. The same procedure was followed for commercial Ti for comparison with the literature to validate the procedure. The surface energy was measured according to Owens–Wendt (Ref 29-31); the surface energy (γ_s) of the solid is equal to the sum of dispersion (γ_s^d) and the polar component (γ_s^p), and the surface energy correlates to the contact angle according to the following equation (Ref 5).

$$(1+\cos\theta)\gamma_L = 2\left(\sqrt{\gamma_1^d\gamma_s^d} + \sqrt{\gamma_1^p\gamma_s^p}\right)$$

The two unknowns, γ_s^d and γ_s^p, were calculated by determining the contact angle of the material using two different liquids (deionized water and glycerol in the current work). The surface tension values $\gamma 1$, γ_1^d, and $\gamma_1^p (\text{in mJ/m}^2)$ for water are 72.8, 21.8 and 51.0, respectively, and the corresponding energies for glycerol are 64, 34, and 33. (Ref 32, 33)

2.4 Electrochemical Corrosion Studies in Artificial Saliva

Electrochemical corrosion experiments including open circuit potential (OCP) monitoring, electrochemical frequency modulation (EFM), and electrochemical impedance spectroscopic (EIS) tests performed using a Gamry Potentiostat/Galvanostat. A classic three-electrode setup was used within a standard glass tube electrochemical cell in which a graphite rod, an SCE and a TNZ specimen (exposed area of 19.6 mm^2) acted as the auxiliary, reference, and working electrodes, respectively. Artificial saliva (pH-5.5), performing as an electrolyte, was prepared based on the composition (Ref 34) 1.0 g urea + 0.795 g $CaCl_2$-$2H_20$ + 0.690 g NaH_2PO_4-H_2O + 0.4 g KCl + 0.4 g NaCl + 0.005 g Na_2S-$9H_2O$ in 1 L of double distilled water. To attain a steady OCP, the specimens were exposed to the artificial saliva solution for 1 h before electrochemical experiments. For EIS measurement, the selected frequency range was from 10^5 Hz to 10^{-3} Hz with the perturbation amplitude of 10 mV and the achievement of 10 points per decade.

EFM measurements were performed by applying a potential perturbation signal with an amplitude of 10 mV, and two sine waves of 2 and 5 Hz were selected. The base frequency was set as 1 Hz with 32 cycles; therefore, the wave form repeats in the next 1 s. When diffusing a corrosive system, which is nonlinear in nature, the resultant current exhibits the applied two frequencies along with additional frequencies, which are the sum, difference, and multiples of the two applied frequencies.

Further, the intermodulation spectra comprise the resultant current allocated to the intermodulation and harmonic current peaks. Using the suitable disciplined procedure, the higher peaks are utilized to directly calculate the parameters, including the corrosion current density (i_{corr}), corrosion rate, Tafel constants (βc and βa), and causality factors (CF2 & CF3). The protection efficiency was assessed using the obtained i_{corr} values based on the following relation:

$$\mathrm{PE}(\%) = \frac{i^{o}_{corr} - i_{corr}}{i^{o}_{corr}}$$

where i^{o}_{corr} and i_{corr} denote the corrosion current densities for bare and treated TNZ specimens, respectively. EFM and EIS data analysis and curve fitting were performed using Gamry EChem Analyst software. All of the above-mentioned tests were reiterated three times, and the average values are displayed.

3. Results and Discussion

3.1 Microstructure and Phase Constitutions

Figure 1 illustrates the XRD patterns of the nitrided and untreated alloys. The patterns for both samples show the formation of the β-phase and the α phase. The percentage of the β phase is greater than that of the α phase. However, the XRD pattern of the laser nitrided sample clearly reveals the formation of a TiN phase (Fig. 1b). Similar phases were also reported for Ti-13Nb-13Zr (Ref 35). The β-phase peak decreases after nitriding, which is ascribed to the formation of TiN (Ref 15). TiN formation occurs due to the diffusion of nitrogen from the surface during the high-pressure gas-assisted heating process (Ref 36). The formation of TiN was also confirmed from a golden yellowish color of the treated sample (Fig. 2).

Figure 3 shows FE-SEM results for the laser nitrided alloy. The photomicrograph shows the presence of a β-Ti matrix surrounded by an α-Ti region, which confirm the results obtained by XRD. The laser nitrided layer extends 9.1 μm beneath the surface (Fig. 3a). The surface of the nitrided alloy shows the development of a micro/nanostructure (Fig. 3b and c). An EDX analysis of the nitrided layer shows that the existence of nitrogen is related to the formation of nitride species at the surface. The coexistence of Ti and N at all of the examined locations confirms the formation of a TiN layer.

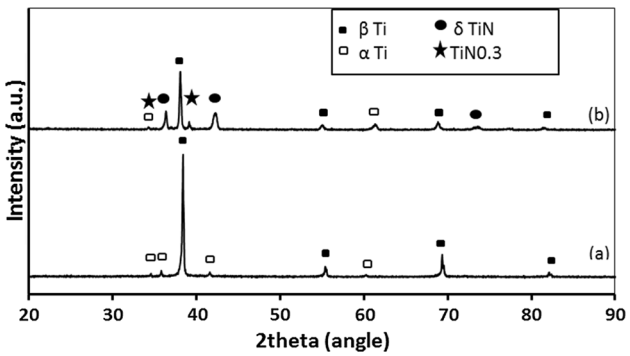

Fig. 1 XRD of (a) an untreated sample and (b) a treated sample

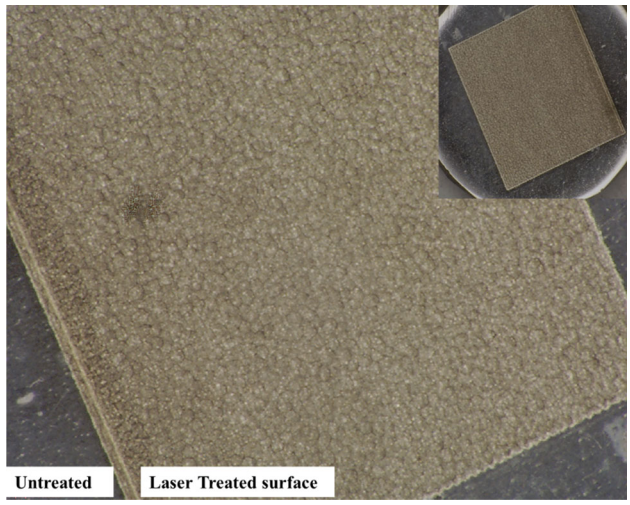

Fig. 2 Optical image of laser nitride and as-received samples

The laser treated sample was also characterized by Raman spectroscopy, and the resulting spectrum is presented in Fig. 4. The spectrum displays two prominent Raman signatures. First, a broad feature is centered at 250 cm^{-1}, with several smaller peaks at 210, 239, 249, 260, 280, and 297 cm^{-1}. The Raman peaks at 211, 230, and 545 cm^{-1} are TiN peaks (Ref 37, 38). A second wide peak is centered at 514 cm^{-1} and ranges from 528 to 576 cm^{-1}, corresponding to TiN (Ref 39). The other two peaks at 239.7 and 280 cm^{-1} are Ti_2O_3 peaks (Ref 37, 38).

The topography of the treated sample surface was characterized using AFM. The surface texture of the laser nitrided sample was composed of fine-sized poles (Fig. 5a and b), and the surface roughness (Ra) was on the order of 13 nm. The root-mean-squared roughness (Rq) was 20.1 nm as shown in Fig. 5(b) and (c).

The hardness of the surface was evaluated by measuring the hardness for both treated and untreated samples. Microhardness measurements showed that the laser nitriding enhanced the hardness of the alloy 2.4-fold. The HV of the nitrided alloy was 1026.9 ± 132; in contrast, the untreated sample had a value of 439.5 ± 10.15. This improvement in the surface hardness is linked to the development of a hard ceramic layer of TiN on the surface. The improvement in hardness will enhance the resistance to wear of the alloy, which will contribute to avoiding the formation of debris that loosens the implant; therefore, the service life of the implant will be improved (Ref 11).

Figure 6 displays the friction coefficient of the untreated and nitrided samples. The results show that laser nitriding reduced the friction coefficient to 0.17, compared to 0.7 for the untreated sample. This reduction is ascribed to the improvement in the surface microhardness of the nitrided alloy (Ref 39). The friction coefficient pattern of the treated sample shows a wave behavior associated with the overlapping of irradiated spots at the surface, which occurred during laser scanning; similar observations have been previously reported (Ref 39, 40).

3.2 XPS Analysis

XPS examination was carried out to characterize the layer formed after laser treatment. XPS survey spectra for the laser

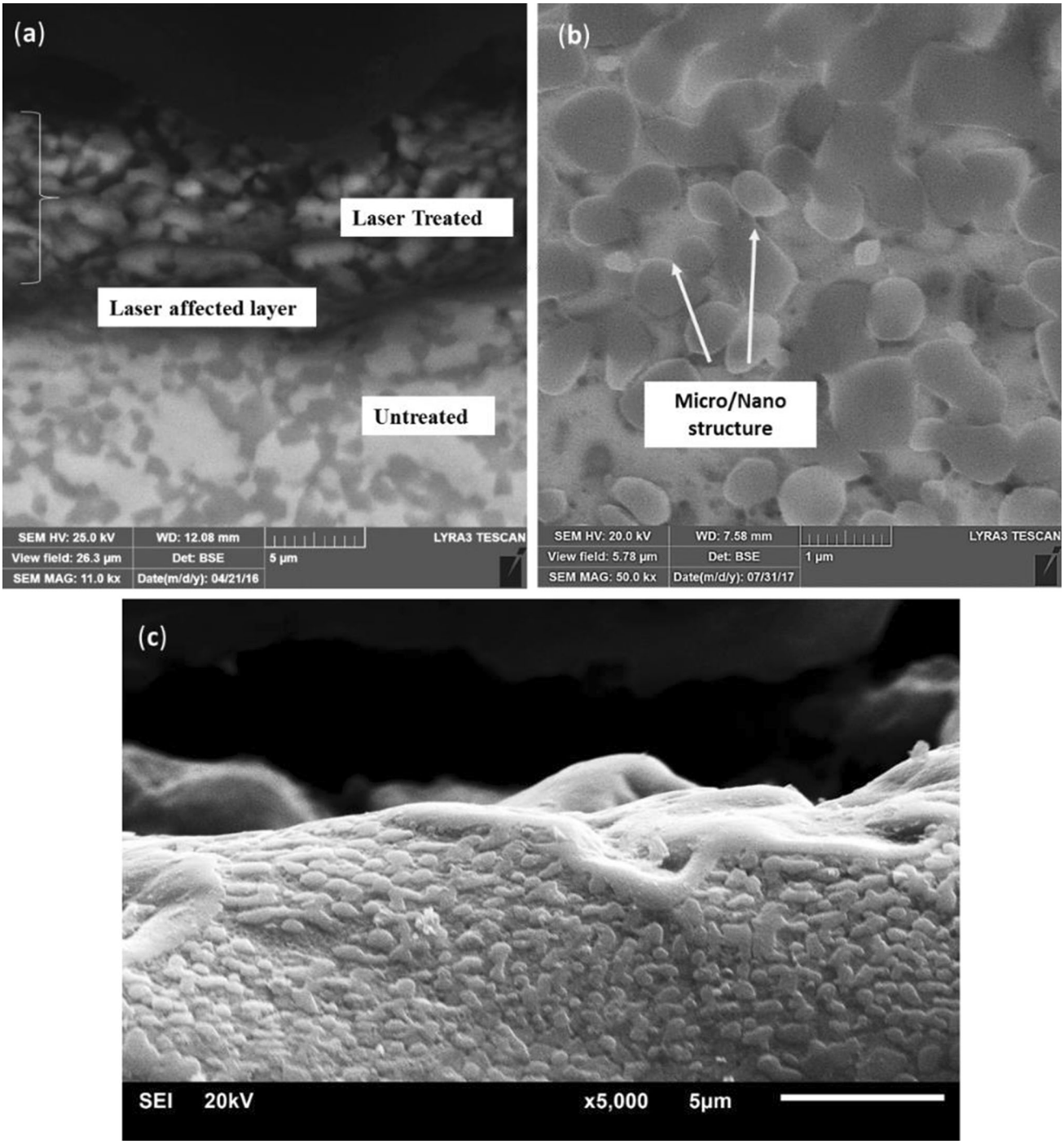

Fig. 3 SEM images of the laser treated sample: (a) microphotographs of the cross section, (b) micro/nano-sized structure formed at the surface, and (c) cross section of the laser nitrided zone with elemental analysis result of (Ti 46.9, Nb 10.2, Zr 8.9, and N 34.1) at.%

nitrided and as-received alloy surfaces are shown in Fig. 7. The primary components of the spectra were indexed according to (Ref 41, 42). Figure 7 shows the XPS survey of the laser nitrided and untreated samples. The Ti peaks in the untreated spectra with binding energies of 457.7 and 454 eV are related to the formation of oxide and metallic phases, respectively. However, for the treated samples, the peak at 456 eV is related to the formation of the nitride phase. Moreover, the spectrum of the treated samples shows a nitrogen peak at 396 eV corresponding to the formation of nitride. These results confirm the presence of a TiN solid solution (Ref 43). The Ti 2p position indicates the presence of a protective TiO2 layer, with a higher percentage exhibited in the untreated samples. The peak intensity decreased after treatment, and its position indicates the presence of TiO2 due to the presence of oxygen in the gas mixture.

3.3 Wettability and Surface Energy

The contact angles of water drops and glycerol on the surface of the treated and untreated alloys were evaluated. The

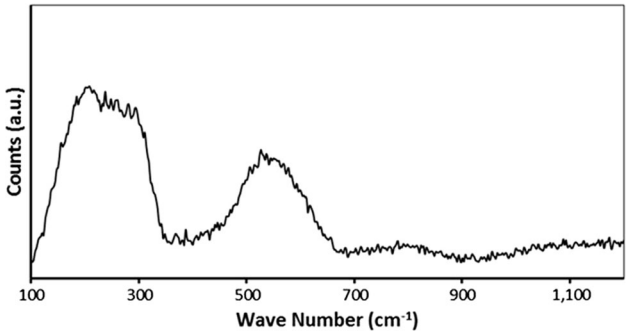

Fig. 4 Raman spectrum for the laser treated sample

surface energies calculated from the contact angles are listed in Table 2. The laser nitriding increased the surface energy of the alloy, and the results indicate that the laser nitriding enhanced the hydrophilicity of the alloy, as evidenced by the decreased contact angle and increased surface energy. These results are in agreement with a similar observation for a Ti-based alloy (Ref 18) and with a previous report (Ref 44) in which TiN was shown to increase the surface energy.

3.4 Electrochemical Corrosion Studies in Artificial Saliva

The OCP of the bare TNZ sample reaches − 220 mV versus SCE after approximately 3600 s of immersion. Initially, the bare TNZ specimen takes ∼ 800 s to reach approximately − 180 mV versus SCE (Fig. 8), a near stable potential. A slight rise in the OCP of bare TNZ to a positive value reveals the growth of a passive film over the TNZ surface and enhancement of the corrosion performance. Then, the OCP value becomes stable after a definite period, representing the stabilization of the passive layer. Several researchers have reported that this steady OCP value was associated with the conversion from TiO or Ti_2O_3 to TiO_2 at the metal/solution interface (Ref 34, 45). However, in contrast, Hitesh D. Vora et al. reported a rapid potential drop in the case of Ti6Al4V in SBF, which might be due to an attack of aggressive Cl^- and breakdown of the passive layer. Further, the rise in OCP is ascribed to the consequent reconstructing of the passive film (Ref 16). The OCP of the laser nitrided TNZ specimen increases more promptly with time at the initial 200 s, representing a compact TiN layer, and then retains a comparatively higher steady value. Moreover, the laser nitrided surface with steadier OCP is associated with an improved microstructure and the existence of an inert TiN phase within the nitrided layer. After treatment by the laser nitriding technique, the OCP

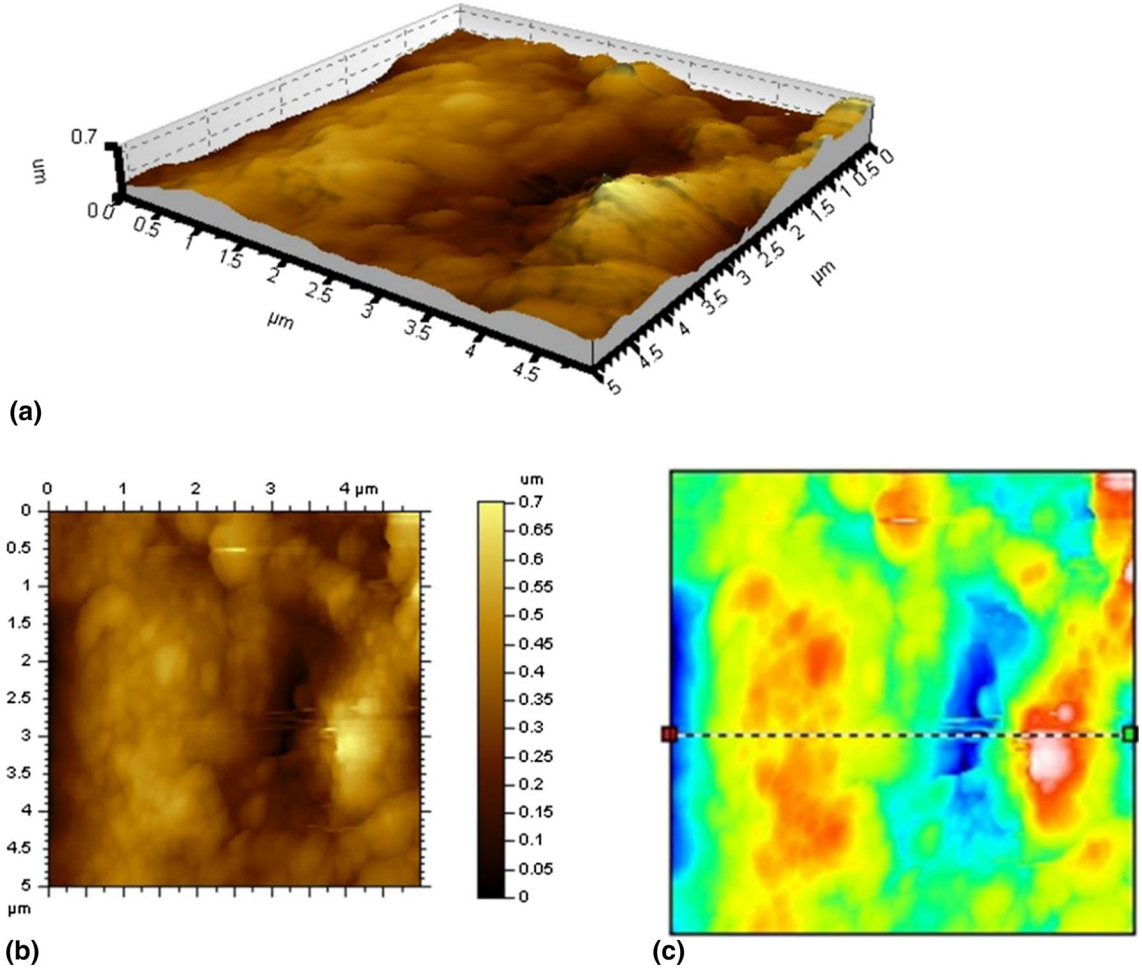

Fig. 5 AFM images of the treated surface showing (a) a 3D topographical image of the surface (b) a 2D topographical image, and (c) an extracted profile

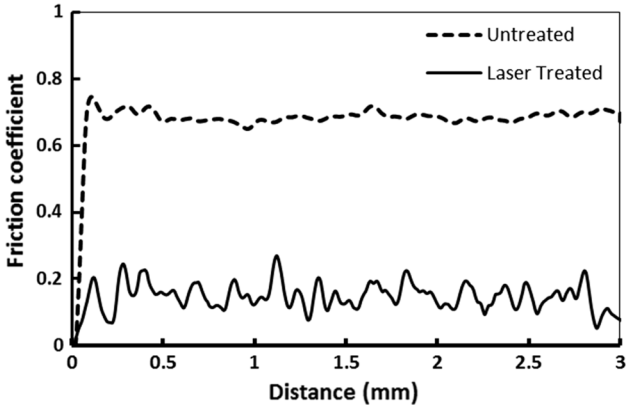

Fig. 6 Friction coefficient of the laser treated and as-received alloy surfaces

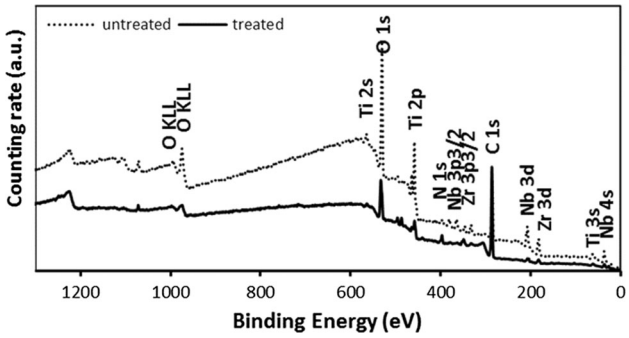

Fig. 7 XPS survey spectra of treated and untreated alloys

of the TNZ specimen was shifted in a more positive direction, which indicates the production of a comparatively thicker and less porous laser nitrided surface on the TNZ substrates with higher thermodynamic stability. Similarly, Singh et al. evaluated the variation in the OCP of bare and laser nitrided Ti-6Al-4V substrates in Ringer's solution and observed that the laser treated samples exhibited more anodic OCP (depending on the laser treatment parameters) than the untreated one (Ref 19).

EFM intermodulation spectra (current response as a function of frequency) obtained from EFM measurements are presented in Fig. 9. The intermediation and harmonic peaks are clearly noticeable and are considerably higher than the background noise. The observed two higher peaks with amplitudes of approximately 100 μA are considered the response to the 2 and 5 Hz (40 and 100 mHz) excitation frequencies, and these peaks have been selected to estimate the i_{corr} and the Tafel constants. Table 3 summarizes the corrosion kinetic parameters, such as the protection efficiency, i_{corr}, CF-2 and CF-3, for bare and laser nitrided TNZ specimens in an artificial saliva medium. As seen in Table 3, the i_{corr} value of TNZ specimens with laser treatment noticeably decreases by at least one order of magnitude, demonstrating the enhanced corrosion protection performance of the laser nitrided TNZ surface due to the

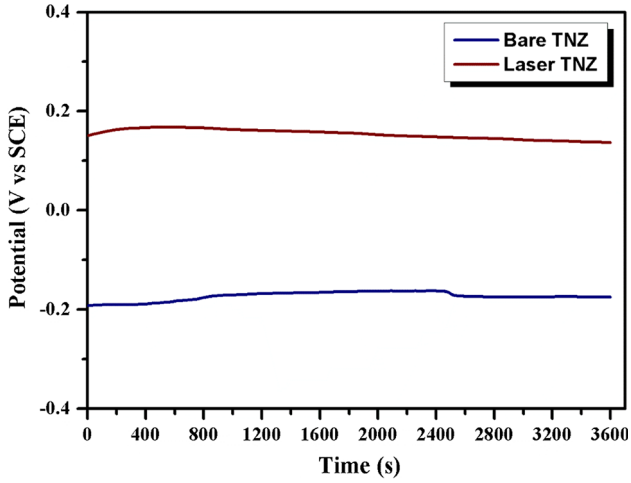

Fig. 8 OCP curves of bare and laser nitrided TNZ specimen in artificial saliva medium

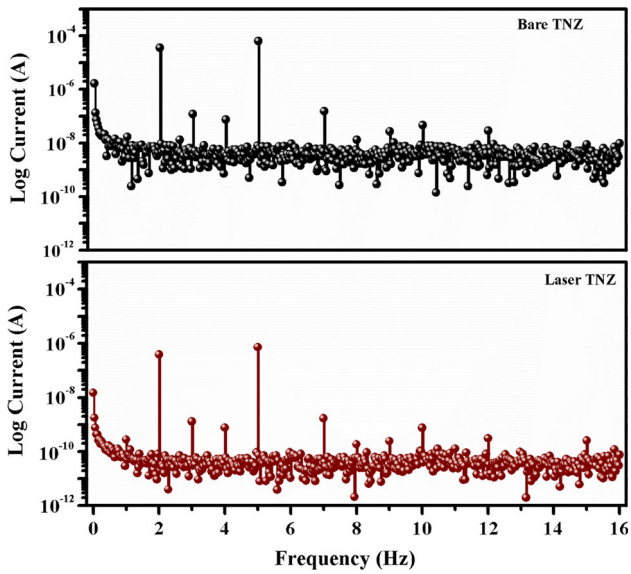

Fig. 9 EFM intermodulation curves for bare and laser nitrided TNZ specimen in artificial saliva medium

presence of a compact and inert TiN layer on the TNZ surface. Chan et al. (Ref 46) evaluated the corrosion performance of laser nitrided Ti-Nb-Zr-Ta (TNZT) alloy in a Hanks' solution and found that the i_{corr} value of treated TNZT alloy is approximately 0.28 μA cm^{-2}. Interestingly, in the present investigation, the i_{corr} value of the treated TNZ substrates in artificial saliva is approximately 1.85×10^{-3} μA cm^{-2}, which is two order of magnitude lower than the former. Moreover, Geetha et al. reported that the TiN surface with nitrogen on the Ti-13Nb-13Zr alloy can combine with oxygen to produce oxynitrides, with the formation of a TiO_2 film that could inhibit

Table 2 Surface energy measurements

Alloy surface	Contact angle for water	Contact angle for glycerol	γ_s^d, mJ m^{-2}	γ_s^p, mJ m^{-2}	γ_s, mJ m^{-2}
Untreated surface	64	67.5	5.01	34.3	39.54
Treated surface	60.2	63.55	5.9	36.4	42.36

Table 3 EFM and EIS circuit parameters for bare and laser treated TNZ specimens

	EFM				EIS						
Substrate	i_{corr} μA cm^{-2} × 10^{-3}	CF2	CF3	Protection efficiency, %	R_s, Ω cm^2	R_{ct}, kΩ cm^2	Q_{dl}, μF cm^{-2}	n_{dl}	R_f, kΩ cm^2	Q_f, μF cm^{-2}	n_f
Bare TNZ	52.97	1.684	1.911	…	158	432.97	24.58	0.90	…	…	…
Laser TNZ	1.85	1.962	2.382	96.50	149	646.98	0.34	0.94	85.77	0.19	0.93

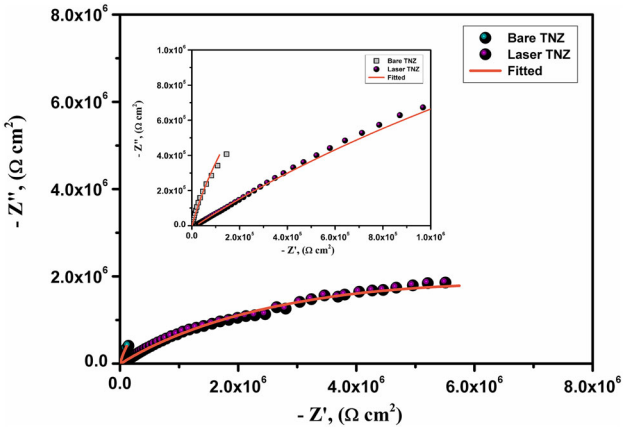

Fig. 10 Nyquist plots for bare and laser nitrided TNZ specimen in artificial saliva medium

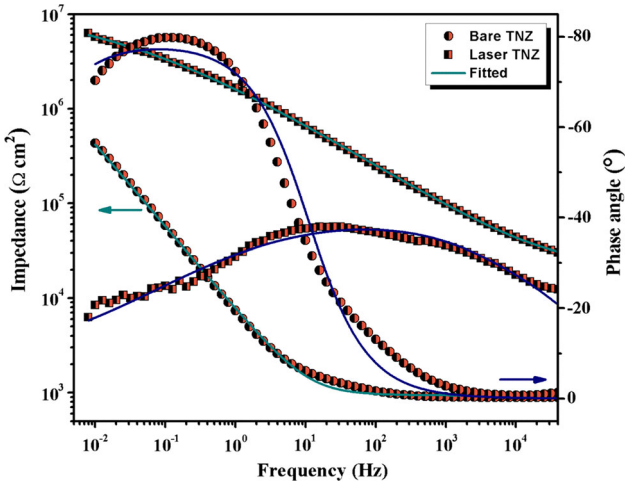

Fig. 11 Bode plots for bare and laser nitrided TNZ specimen in artificial saliva medium

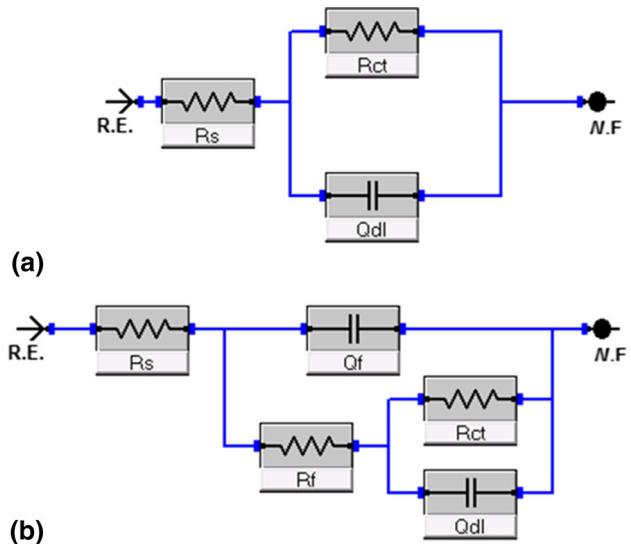

Fig. 12 EIS circuit diagrams for (a) bare and (b) laser nitrided TNZ specimen in artificial saliva medium

the leaching of Ti, which would improve the surface protection against corrosion. Moreover, the alloying constituents, such as Nb and Zr, also facilitate the anticorrosion performance of the passive layer (Ref 47). In general, the causality factors serve as an inner assessment on the authenticity of the values obtained from EFM measurements. When the values of CF vary considerably from the hypothetical values of 2 and 3, it can be assumed that the experimentations are biased by noise. From Table 3, it could be understood that the values of CF2 and CF3 were nearly equivalent to the theoretical values of 2 and 3, demonstrating the reliability of the obtained experimental data due to the fundamental correlation concerning the response and perturbation signal. Furthermore, the PE value of the laser nitrided TNZ specimen was found to be 96.50%, which further confirmed the enhanced corrosion resistant behavior of the TiN layer on the TNZ specimen in artificial saliva medium. Hitesh D. Vora et al. (Ref 16) also evaluated the PE of laser nitrided Ti-6Al-4V substrates in SBF, and it was found to be 71% and to increase with the laser energy density.

EIS was performed to validate the results of the OCP and EFM experiments. The EIS data of the substrate and nitrided specimens immersed in artificial saliva medium are displayed in Nyquist (Fig. 10) and Bode (Fig. 11) formats. Nyquist plots of bare and laser nitrided TNZ specimens are described by an imperfect and distorted arc; a capacitive performance of a passive layer and certain distortions linked to a dual layer could be detected in the case of the treated TNZ specimen (Ref 48). It is well established that the diameter of the capacitive arc in the Nyquist plot indicates the resistance shown by the surface to corrosion, and a larger diameter frequently represents enhanced corrosion performance (Ref 49, 50). The radius of curvature of the capacitance arc of the laser nitrided TNZ was the largest compared to that of the bare specimen, indicating that the corrosion protection performance of TNZ increased with laser nitriding owing to the production of a dense TiN film.

From the preliminary observation of the Bode graphs (Fig. 11), the laser treated TNZ specimen shows different EIS curves compared to the bare TNZ. For bare TNZ, a large phase angle of approximately − 80° continued to be observed in the mid- and low-frequency regions, while the slope of the resistant curves was found to be approximately − 1, representing the

distinctive result of the capacitive behavior of the native passive layer (Ref 51). Conversely, two maxima in the phase angle were observed in the high and low-frequency regions in the case of laser nitrided TNZ specimens, which reveals the association of at least two time constants related to the two-layer structure of the laser treated TNZ specimen.

To obtain quantitative evidence of the corrosion resistant behavior of laser treated TNZ specimens, EIS circuit fitting was performed by selecting appropriate equivalent circuit diagrams, which are displayed in Fig. 12. In the selected EIS circuit diagram, R_s and R_{ct} denote the electrolytic and charge transfer resistance in parallel to the constant phase element (CPE_{dl}). R_f and CPE_f denote the resistance and constant phase element, and these were incorporated to justify the capacitance and resistance related to the TiN film formed over the TNZ surface. Since the capacitance in EIS often performs non-ideally because of the complex corrosion phenomenon at the interface, CPE as stated above, demonstrating a deviation from a perfect capacitor, was employed. The impedance of CPE is represented as $Z_{CPE} = [Q(j\omega)^n]^{-1}$, where Q denotes the capacitance value of the passive film. $j\omega$ denotes the complex variable for sinusoidal perturbations, with $\omega = 2\pi f$, and n is the exponent of CPE ranging from -1 to 1, which is linked to the heterogeneous current distribution because of the surface roughness or inhomogeneity.

Table 3 summarizes the EIS parameters of bare and treated TNZ specimens. Based on Table 3, the laser nitrided TNZ specimen revealed noble barrier performance by exhibiting a film resistance R_f of 85 kΩ cm^2 and an increase in the R_{ct} value from 432 kΩ cm^2 for bare TNZ to 646 kΩ cm^2. Moreover, the

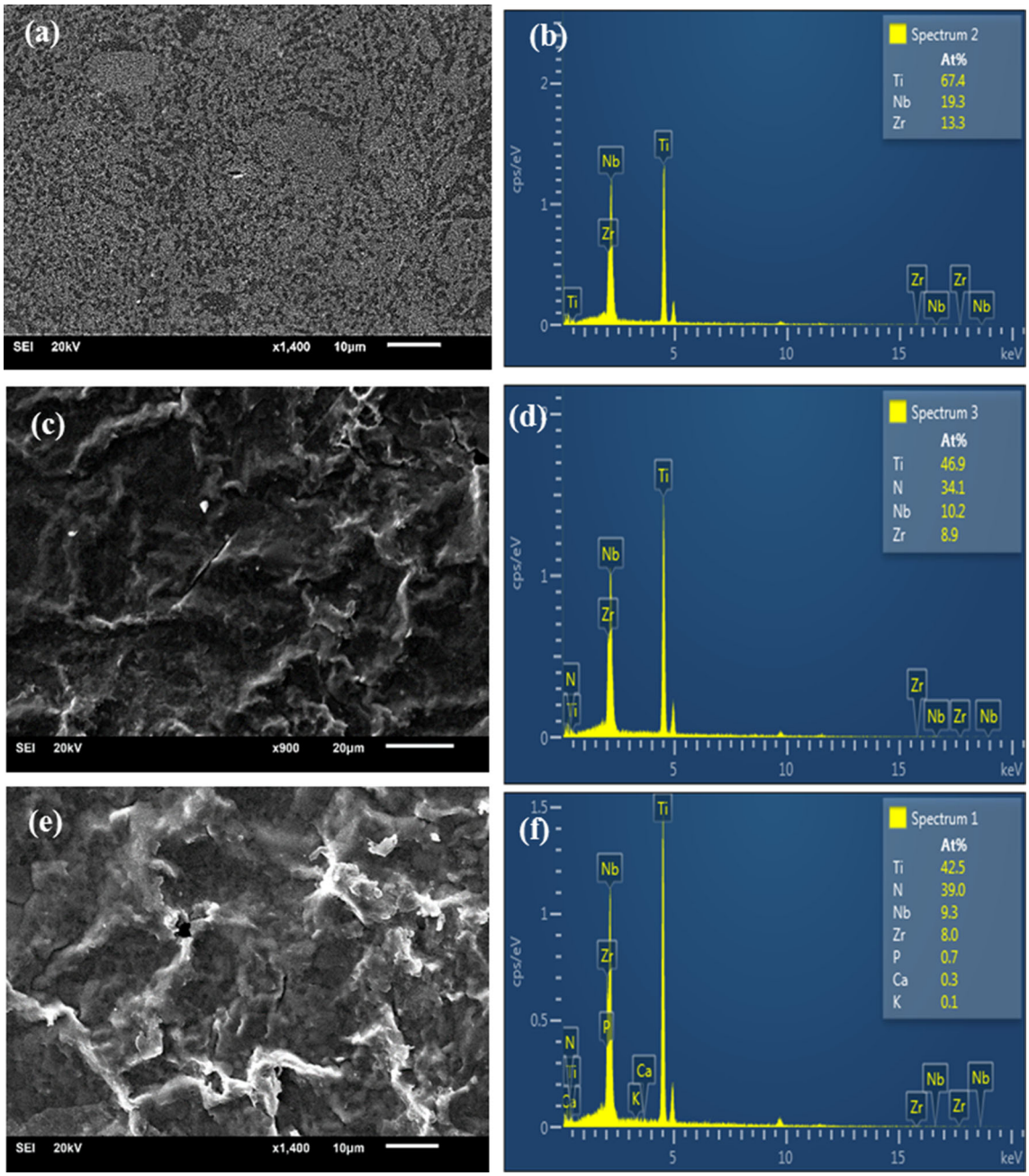

Fig. 13 SEM and EDX elemental analysis for untreated surface (a, b), laser nitrided surface (c, d), and corroded test area (e, f)

laser nitrided TNZ specimen showed a reduction in the CPE_{dl} value (0.34 μF cm^{-2}) on the order of two degree, representing a significant lessening in permeation of the destructive elements from artificial saliva medium. Zhao et al. (Ref 52) recently compared the corrosion behavior of laser nitrided Ti-35Nb-7Zr-5Ta (TNZT) alloys prepared with Ar or N_2 gas in SBF medium and reported that the laser nitrided surface prepared in N_2 exhibited the highest total impedance value of 173.90 kΩ cm^{-2}, whereas the values were found to be 8.43 kΩ cm^{-2} for the bare alloy and 12.99 kΩ cm^{-2} for the TNZT alloy processed in Ar. Manhabosco et al. (Ref 17) also evaluated the corrosion resistance of nitrided Ti6Al4V in SBF medium and found that the CPE_{dl} values of nitrided Ti6Al4V were found to be approximately 51 and 64 μF cm^{-2} for days 1 and 23 of immersion, respectively. Therefore, the noteworthy results regarding the electrochemical corrosion performance of laser nitrided TNZ specimens compared to bare specimens were revealed in the larger capacitive arcs. Higher R_{ct} existed with lower CPE_{dl} and i_{corr} values, all of which confirmed the effectiveness and strength of the compact laser treated surface for enhancing the corrosion protection of TNZ alloy. In contrast, Sathish et al. (Ref 17) reported that the surface protective performance of laser nitrided Ti13Nb13Zr (TNZ) substrates against corrosion in Hank solution was observed to be lower than that of the bare TNZ alloy and Cp Ti substrates. They also explained that the TiN dendrite behavior produced on TNZ alloy is less compact and more scattered in comparison with TiN produced on Cp Ti substrates. Further, previous research on corrosion investigations of laser nitrided TNZ alloy prepared at a low scanning speed showed higher corrosion resistance in comparison with the bare alloy. Therefore, it could be obviously understood that an optimum quantity of TiN is needed to enhance the corrosion resistance, below which surface protection against corrosion will not be improved though the substrate is laser treated.

To validate the electrochemical corrosion results in artificial saliva, the surface morphology of laser nitrided TNZ substrates before and after corrosion tests was examined using SEM/EDS analysis. Figure 13(c) and (d) provides the surface morphologies and compositions of the laser nitrided TNZ substrates after corrosion tests in artificial saliva compared to untreated sample in Fig. 13(a) and (b). Consistent results are observed between the SEM and electrochemical corrosion results mentioned above. Slight cracks and spallation can be identified in the laser nitrided surface after the corrosion tests; however, the surface of the laser nitrided TNZ maintained its integrity. Furthermore, surface pits were not observed in the SEM image. EDS results for the laser nitrided TNZ substrates before and after corrosion tests are presented in Fig. 13(e) and (f). EDS spectra after the corrosion test exhibited strong peaks for Ti, N, Nb, and Zr from the base TNZ substrate and for laser nitrided TiN with very trace quantities of Ca, K, and P from saliva. Comparing the SEM images with the EDS spectra, it can be concluded that the laser nitrided surfaces significantly protected the TNZ substrates against corrosion in artificial saliva medium.

4. Conclusion

Laser gas nitriding was applied to enhance the surface characteristics and corrosion protection of Ti-20Nb-13Zr at.% alloy in artificial saliva for dental applications. The treated alloy was characterized using XRD, XPS, Raman spectroscopy, FE-SEM, EDXAFM and microhardness, scratch, and surface energy measurements. The results show the formation of a TiN layer on the alloy surface. An examination of the microstructure shows that the thickness of the nitrided layer extends relatively uniformly below the surface to a depth of 9.1 μm. The nitride layer formed on the surface leads to a 2.4-fold improvement of the surface hardness of the nitrided sample relative to the hardness of the untreated surface. The scratch tests show that the friction coefficient of the laser nitrided samples is lower than that of the untreated sample surface; this difference is attributed to a uniformly distributed elemental composition, microhardness enhancement, and TiN formation at the surface of the laser nitrided sample. Contact angle measurements and surface energy analysis showed that the laser nitriding improved the hydrophilicity and surface energy of the alloy. Corrosion analysis showed an improvement in the corrosion protection of TNZ alloy based on the large capacitive arc, higher R_{ct} with lower CPEdl value, and lower i_{corr} value with higher protection efficiency in artificial saliva medium. It can be concluded that laser treatment would be a potentially successful surface modification process for Ti alloys for dental applications.

Acknowledgment

The authors would like to acknowledge the support provided by King Fahd University of Petroleum and Minerals, Project No. #IN151013.

References

1. A.L.R. Ribeiro, R.C. Junior, F.F. Cardoso, R.B. Fernandes Filho, and L.G. Vaz, Mechanical, Physical, and Chemical Characterization of Ti-35Nb-5Zr and Ti-35Nb-10Zr Casting Alloys, *J. Mater. Sci. Mater. Med.*, 2009, **20**(8), p 1629–1636
2. K. Niespodziana, K. Jurczk, and M. Jurczk, The Synthesis of Titanium Alloys for Biomedical Applications, *Rev. Adv. Mater. Sci.*, 2008, **18**, p 236–240
3. V.A.R. Henriques, E.T. Galvani, S.L.G. Petroni, M.S.M. Paula, and T.G. Lemos, Production of Ti-13Nb-13Zr Alloy for Surgical Implants by Powder Metallurgy, *J. Mater. Sci.*, 2010, **45**(21), p 5844–5850
4. N. Schiff, B. Grosgogeat, M. Lissac, and F. Dalard, Influence of Fluoride Content and pH on the Corrosion Resistance of Titanium and Its Alloys, *Biomaterials*, 2002, **23**(9), p 1995–2002
5. A. Biesiekierski, J. Wang, M.A.H. Gepreel, and C. Wen, A New Look at Biomedical Ti-Based Shape Memory Alloys, *Acta Biomater.*, 2012, **8**(5), p 1661–1669
6. M.A. Hussein, C. Suryanarayana, M.K. Arumugam, and N. Al-Aqeeli, Effect of Sintering Parameters on Microstructure, Mechanical Properties and Electrochemical Behavior of Nb-Zr Alloy for Biomedical Applications, *Mater. Des.*, 2015, **83**, p 344–351
7. M.A. Hussein, C. Suryanarayana, and N. Al-Aqeeli, Fabrication of Nano-grained Ti-Nb-Zr Biomaterials Using Spark Plasma Sintering, *Mater. Des.*, 2015, **87**, p 693–700
8. M.O. Alam and A.S.M.A. Haseeb, Response of Ti-6Al-4V and Ti-24Al-11Nb Alloys to Dry Sliding Wear Against Hardened Steel, *Tribol. Int.*, 2002, **35**(6), p 357–362
9. M.A. Khan, R.L. Williams, and D.F. Williams, In-Vitro Corrosion and Wear of Titanium Alloys in the Biological Environment, *Biomaterials*, 1996, **17**(22), p 2117–2126
10. P.G. Liang, A. Ferguson, and E.S. Hodge, Tissue Reaction in Rabbit Muscle Exposed to Metallic Implants, *J. Biomed. Mater. Res.*, 1967, **1**(1), p 135–149

11. M.A. Hussein, A.S. Mohammed, and N. Al-Aqeeli, Wear Characteristics of Metallic Biomaterials: A Review, *Materials*, 2015, **8**(5), p 2749–2768
12. M.A. Hussein, A.M. Kumar, B.S. Yilbas, and N. Al-Aqeeli, Laser Nitriding of the Newly Developed Ti-20Nb-13Zr at.% Biomaterial Alloy to Enhance Its Mechanical and Corrosion Properties in Simulated Body Fluid, *J. Mater. Eng. Perform.*, 2017, **26**(11), p 5553–5562
13. Z.A. Uwais, M.A. Hussein, M.A. Samad, and N. Al-Aqeeli, Surface Modification of Metallic Biomaterials for Better Tribological Properties: A Review, *Arab. J. Sci. Eng.*, 2017, **42**(11), p 4493–4512
14. T.M. Manhabosco, S.M. Tamborim, C.B. Dos Santos, and I.L. Müller, Tribological, Electrochemical and Tribo-Electrochemical Characterization of Bare and Nitrided Ti6Al4V in Simulated Body Fluid Solution, *Corros. Sci.*, 2011, **53**(5), p 1786–1793
15. S. Sathish, M. Geetha, N.D. Pandey, C. Richard, and R. Asokamani, Studies on the Corrosion and Wear Behavior of the Laser Nitrided Biomedical Titanium and Its Alloys, *Mater. Sci. Eng. C*, 2010, **30**(3), p 376–382
16. H.D. Vora, R.S. Rajamure, S.N. Dahotre, Y.-H. Ho, R. Banerjee, and N.B. Dahotre, Integrated Experimental and Theoretical Approach for Corrosion and Wear Evaluation of Laser Surface Nitrided, Ti-6Al-4V Biomaterial in Physiological Solution, *J. Mech. Behav. Biomed. Mater.*, 2014, **37**, p 153–164
17. T.M. Manhabosco, S.M. Tamborim, C.B. dos Santos, and I.L. Müller, Tribological, Electrochemical and Tribo-electrochemical Characterization of Bare and Nitrided Ti6Al4V in Simulated Body Fluid Solution, *Corros. Sci.*, 2011, **53**(5), p 1786–1793
18. C.-H. Ng, C.-W. Chan, H.-C. Man, D. Waugh, and J. Lawrence, Modifications of Surface Properties of Beta Ti by Laser Gas Diffusion Nitriding, *J. Laser Appl.*, 2016, **28**(2), p 022505
19. M. Geetha, U.K. Mudali, N.D. Pandey, R. Asokamani, and B. Raj, Microstructural and Corrosion Evaluation of Laser Surface Nitrided Ti-13Nb-13Zr Alloy, *Surf. Eng.*, 2004, **20**(1), p 68–74
20. H.C. Man, Q. Wang, and X. Guo, Laser Surface Microdrilling of Ti and Laser Gas Nitrided Ti for Enhancing Fixation of Dental Implants, *Opt. Lasers Eng.*, 2010, **48**(5), p 583–588
21. F. Torregrosa, L. Barrallier, and L. Roux, Phase Analysis, Microhardness and Tribological Behaviour of Ti-6Al-4V After Ion Implantation of Nitrogen in Connection with Its Application for Hip-Joint Prosthesis, *Thin Solid Films*, 1995, **266**(2), p 245–253
22. S. Shimadaa, T.Y. Takadaa, and J. Tsujino, Deposition of TiN Films on Various Substrates from Alkoxide Solution by Plasma-Enhanced CVD, *Surf. Coat. Technol.*, 2005, **199**(1), p 72–76
23. P. Jiang, X.L. He, X.X. Li, L.G. Yu, and H.M. Wang, Wear Resistance of a Laser Surface Alloyed Ti-6Al-4V Alloy, *Surf. Coat. Technol.*, 2000, **130**(1), p 24–28
24. I. Garcia and J.J. De Damborenea, Corrosion Properties of TiN Prepared by Laser Gas Alloying of Ti and Ti6Al4V, *Corros. Sci.*, 1998, **40**(8), p 1411–1419
25. M.A. Arenas, T.J. Tate, A. Conde, and J. De Damborenea, Corrosion Behaviour of Nitrogen Implanted Titanium in Simulated Body Fluid, *Br. Corros. J.*, 2000, **35**(3), p 232–236
26. A.L. Paschoal, E.C. Vanâncio, L.D.C.F. Canale, O.L.D. Silva, D. Huerta-Vilca, and A.D.J. Motheo, Metallic Biomaterials TiN-Coated: Corrosion Analysis and Biocompatibility, *Artif. Organs*, 2003, **27**(5), p 461–464
27. B.S. Yilbas, N. Al-Aqeeli, and C. Karatas, Laser Control Melting of Alumina Surfaces with Presence of B4C Particles, *J. Alloys Compd.*, 2012, **539**, p 12–16
28. B.S. Yilbas, S.S. Akhtar, and C. Karatas, Laser Carbonitriding of Alumina Surface, *Opt. Lasers Eng.*, 2011, **49**(3), p 341–350
29. T. Senturk Parreidt, M. Schmid, and C. Hauser, Validation of a Novel Technique and Evaluation of the Surface Free Energy of Food, *Foods*, 2017, **6**(4), p 31
30. X. Lu, Z. Zhao, and Y. Leng, Biomimetic calcium phosphate coatings on nitric-acid-treated titanium surfaces, *Mater. Sci. Eng. C*, 2007, **27**(4), p 700–708
31. Z. Zhong et al., Surface Energy for Electroluminescent Polymers and Indium-Tin-Oxide, *Appl. Surf. Sci.*, 2003, **207**(1), p 183–189
32. X.J. Wang et al., Apatite-Inducing Ability of Titanium Oxide Layer on Titanium Surface: The Effect of Surface Energy, *J. Mater. Res.*, 2008, **23**(6), p 1682–1688
33. Q. Zhao, Y. Liu, and E.W. Abel, Effect of Temperature on the Surface Free Energy of Amorphous Carbon Films, *J. Colloid Interface Sci.*, 2004, **280**(1), p 174–183
34. M.V. Popa, I. Demetrescu, E. Vasilescu, P. Drob, A.S. Lopez, J. Mirza-Rosca, C. Vasilescu, and D. Ionita, Corrosion Susceptibility of Implant Materials Ti-5Al-4V and Ti-6Al-4Fe in Artificial Extra-Cellular Fluids, *Electrochim. Acta*, 2004, **49**(13), p 2113–2121
35. D.Y. Kwok, The Usefulness of the Lifshitz–van der Waals/Acid–Base Approach for Surface Tension Components and Interfacial Tensions, *Colloids Surf. A*, 1999, **156**(1), p 191–200
36. B.S. Yilbas, H. Ali, and C. Karatas, [INVITED] Laser Gas Assisted Treatment of Ti-Alloy: Analysis of Surface Characteristics, *Opt. Laser Technol.*, 2016, **78**, p 159–166
37. C.P. Constable, J. Yarwood, and W.-D. Münz, Raman Microscopic Studies of PVD Hard Coatings, *Surf. Coat. Technol.*, 1999, **116**, p 155–159
38. S.H. Shin, R.L. Aggarwal, B. Lax, and J.M. Honig, Raman Scattering in Ti2O3-V2O3 alloys, *Phys. Rev. B*, 1974, **9**(2), p 583
39. B.S. Yilbas, H. Ali, N. Al-Aqeeli, and C. Karatas, [INVITED] Laser Treatment of Inconel 718 Alloy and Surface Characteristics, *Opt. Laser Technol.*, 2016, **78**, p 153–158
40. B.S. Yilbas and H. Ali, Laser Texturing of Hastelloy C276 Alloy Surface for Improved Hydrophobicity and Friction Coefficient, *Opt. Lasers Eng.*, 2016, **78**, p 140–147
41. J.F. Moulder, W.F. Stickle, P.E. Sobol, and K.D. Bomben, *Handbook of X-ray Photoelectron Spectroscopy*, Physical Electronics USA Inc., Chamhassen, 1995
42. A.V. Naumkin, A. Kraut-Vass, S.W. Gaarenstroom, and C.J. Powell, NIST X-ray photoelectron spectroscopy database, in *NIST Standard Reference Database 20*, version 4.1, US Secretary of Commerce on behalf of the United States of America (2012)
43. M.S. Selamat, T.N. Baker, and L.M. Watson, Study of the Surface Layer Formed by the Laser Processing of Ti-6Al-4V Alloy in a Dilute Nitrogen Environment, *J. Mater. Process. Technol.*, 2001, **113**(1), p 509–515
44. A. Amadeh, S. Heshmati-Manesh, J.C. Labbe, A. Laimeche, and P. Quintard, Wettability and Corrosion of TiN, TiN-BN and TiN-AlN by Liquid Steel, *J. Eur. Ceram. Soc.*, 2001, **21**(3), p 277–282
45. C.E.B. Marino, E.M. Oliveira, R.C. Rocha-Fliho, and S.R. Biaggio, On the Stability of Thin-Anodic-Oxide Films of the Titanium in Acid Phosphoric Media, *Corros. Sci.*, 2001, **43**(8), p 1465–1476
46. C.-W. Chan, S. Lee, G. Smith, G. Sarri, C.-H. Ng, A. Sharba, and H.-C. Man, Enhancement of Wear and Corrosion Resistance of Beta Titanium Alloy by Laser Gas Alloying with Nitrogen, *Appl. Surf. Sci.*, 2016, **367**, p 80–90
47. M. Geetha, U. Kamachi Mudali, N.D. Pandey, R. Asokamani, and B. Raj, Microstructural and Corrosion Evaluation of Laser Surface Nitrided Ti-13Nb-13Zr Alloy, *Surf. Eng.*, 2004, **20**, p 68–74
48. C. Vasilescu, S.I. Drob, E.I. Neacsu, and J.C. Mirza Rosca, Surface Analysis and Corrosion Resistance of a New Titanium Base Alloy in Simulated Body Fluids, *Corros. Sci.*, 2012, **65**, p 431–440
49. Q. Wan, H. Ding, M.I. Yousaf, Y.M. Chen, H.D. Liu, L. Hu, and B. Yang, Corrosion Behaviors of TiN and Ti-Si-N (with 2.9 at.% and 5.0 at.% Si) Coatings by Electrochemical Impedance Spectroscopy, *Thin Solid Films*, 2016, **616**, p 601–607
50. A. Ray, I. Mukhopadhyay, R. Pati, Y. Hattori, U. Prakash, Y. Ishii, and S. Kawasaki, Optimization of Photoelectrochemical Performance in Chemical Bath Deposited Nanostructured CuO, *J. Alloys Compd.*, 2017, **695**, p 3655–3665
51. I. Cvijović-Alagić, Z. Cvijović, J. Bajat, and M. Rakin, Composition and Processing Effects on the Electrochemical Characteristics of Biomedical Titanium Alloys, *Corros. Sci.*, 2014, **83**, p 245–254
52. X. Zhao, P. Zhang, X. Wang, Y. Chen, H. Liu, L. Chen, Y. Sheng, and W. Li, In-Situ Formation of Textured TiN Coatings on Biomedical Titanium Alloy by Laser Irradiation, *J. Mech. Behav. Biomed. Mater.*, 2017, **78**, p 143–153